



## INTRODUCTION

The eukaryotic cell's nucleus contains numerous genes arranged on chromosomal DNA. This compact environment houses dense genetic material and various nuclear bodies. The control and processing of genetic information rely on proteins' ability to locate specific DNA sequences within the crowded nucleus, which is influenced by its structure and dynamics. Previous studies have extensively examined the dynamics of single nucleus entities [1–6]. These studies have revealed the ultra-slow movement caused by crowding. Typically, measurements of single particle dynamics in the nucleus involve either time or ensemble averages, which overlook important information and correlations. This research aims to uncover these correlations using multiple methods, particularly by simultaneously tracking many individual particles. This approach allows us to gain insights into directional correlations within a path, as well as pair-wise correlation functions. Additionally, this investigation sheds light on patchy dynamics within the nucleus, where motion is correlated within specific patches.

Zidovska and colleagues [7] developed a potent technique called displacement correlation spectroscopy (DCS) to map the dynamics of large-scale correlated chromatin movements. They found that the motion of chromatin regions ( $4 - 5 \mu\text{m}$ ) was coherent for several seconds. In our study, we focus on investigating the motion of individual telomeres. The coherent motion of chromatin territories reveals how different nucleus regions communicate and respond to DNA damage [4]. Nonetheless, it remains unclear how this large-scale coherent motion affects individual molecules.

Telomeres are specialized DNA sequences present at the cap of chromosomes in eukaryotic cells that prevent their degradation and fusion with other chromosomes. In this study, we analyze the movement of individual telomeres to elucidate the dynamics of chromatin loci and their interrelations. We focus on two types of correlations: self-correlation along the telomere path and correlation between pairs of telomeres. How do these correlations manifest in the behavior of telomeres, and how can they be manipulated in experimental settings? Our study shows that Lamin-A, a critical protein for nuclear organization, controls the extent and nature of these crucial correlations.

Studies on the dynamics of single molecules in the cellular environment have shown that their behavior is primarily governed by caging [2, 4, 8], leading to anti-persistent motion, although active forces can induce persistent or directional motion [1]. Our work reveals

that both types of behavior occur in telomeres within the cell nucleus and that Lamin-A plays a role in their regulation. Despite previous progress, the presence of spatially coherent structures implies that correlations may exist between the dynamics of pairs of particles. Our study addresses this challenge by showing that chromatin loci such as telomeres must be treated collectively, as many-body correlations are present.

This investigation involves studying the dynamics of telomeres in two different types of cells: wild-type cells (WT) that express Lamin A and cells where Lamin A is knocked out and is not expressed (KO). Our findings show that telomeres in KO cells exhibit persistent motion, which is absent in WT cells with intact Lamin-A. We also discover that the pairwise correlation between particles is associated with the persistent motion of individual telomeres. These results emphasize the importance of Lamin-A in regulating chromatin dynamics and reveal the collective behavior of telomeres in the nucleus.

Lamin-A is a crucial component of the nuclear lamina, providing essential structural support to the nucleus and various factors, such as age, stress, and disease, can influence its expression [9–11]. Dysregulation of Lamin-A expression has been linked to a range of pathological conditions, collectively called laminopathies [12]. Our research demonstrates that in KO cells, the magnitude of the telomere dynamics is significantly greater than in WT cells. In particular, we observe that in the absence of Lamin-A, telomeres can move persistently over considerable distances, up to 20% of the nucleus diameter. It indicates that low levels of Lamin-A can disrupt the dynamics in the whole volume of the nucleus by considerably modifying the active dynamics.

## **RESULTS**

### **Experimental setup**

Measurements were carried out in cell lines of mouse embryonic fibroblasts (MEFs), one that is KO and their WT [13]. They were kindly provided by Prof. Susana Gonzalo from Saint Louis University School of Medicine, St Louis, MO, USA. The cells were maintained in Dulbecco’s high-glucose modified Eagle’s medium containing 10% fetal bovine serum, 1% penicillin and streptomycin antibiotics and 1% L-glutamine, all materials are from Biological Industries, Beit HaEmek, Israel.

For telomere tracking, we used transient labeling of the shelterin subunit TRF2 fused to green fluorescent protein (GFP), a kind gift from Prof. Sabine Mai (Manitoba Institute of Cell Biology, Winnipeg University, Canada). The imaging system includes an inverted Olympus IX-81 fluorescence microscope coupled to an FV-1000 confocal set-up (Olympus, Tokyo, Japan), and a UPLSAPO X60 objective lens (NA=1.35). Cells were placed in a 37°C incubator (Tokai, Shizuoka-ken, Japan) with a 5%  $CO_2$  level. The measurements were performed in three dimensions to correct for cell linear and rotational drift, although the actual dynamic analysis was performed only on the planar  $xy$  motion, see details below. Normally 35 equally spaced planes were measured with a lag time of 18.5 seconds, a voxel size of 108 X 108 X 350  $nm^3$  and 50 or 100 time-points. The planar resolution of our measurements is 170 nm, and the spatial precision is better than 10 nm (localization error), based on both calculation and measurement of a fixed sample. Finally, Quantitative single particle tracking (SPT) analysis of time-lapse image sequences was performed.

### Correction of linear and rotational drift.

As mentioned above we employed confocal microscopy to obtain 3D data sets of telomere's trajectories. As the cells are alive, they tend to move during the data acquisition. In order to describe the motion of telomeres with respect to the nucleus, the nucleus motion has to be subtracted from the telomere's trajectories. Indeed, the observation of telomere dynamics before and after corrections reveals that it is necessary to rectify the translational drift, and also but less importantly the nucleus rotation (Supplementary Material Fig. S1).

We now explain how to correct telomere trajectories from cell motion, this is particularly important as we wish to explore the correlations between pairs of telomeres. To see how the drift of each different cell behaves with time ( $t_i$ ), we computed the drift vector  $\vec{R}(t_i) = (R_x(t_i), R_y(t_i))$ , where each component is the respective average center of mass:  $R_x(t_i) = \sum_{j=1}^M x^j(t_i)/M$ , and  $R_y(t_i) = \sum_{j=1}^M y^j(t_i)/M$ , (where  $j = 1, \dots, M$  and  $M$  is the number of tracked telomeres in the nucleus). Fig. 1 *a-b*) shows the relative magnitude of the drift vector  $|\vec{R}(t)| - |\vec{R}(t_0)|$  as a function of time, with  $|\vec{R}(t_i)| = \sqrt{R_x^2 + R_y^2}$ , for few cells in both WT and KO cells. The relative drift vector indicates the translational drift of the nucleus. In all cases the relative magnitude of the drift vector follows a smooth nearly linear behavior with time. More precisely, for twelve different cells displayed (8 WT and 4 KO), we observe that

seven of them (60%) has almost zero drift and the others cells exhibit a quasi-monotonous trend with slope close to  $\sim 0.1$ , *i.e.*  $\sim \pm 0.005 \mu\text{m}/\text{s}$ .

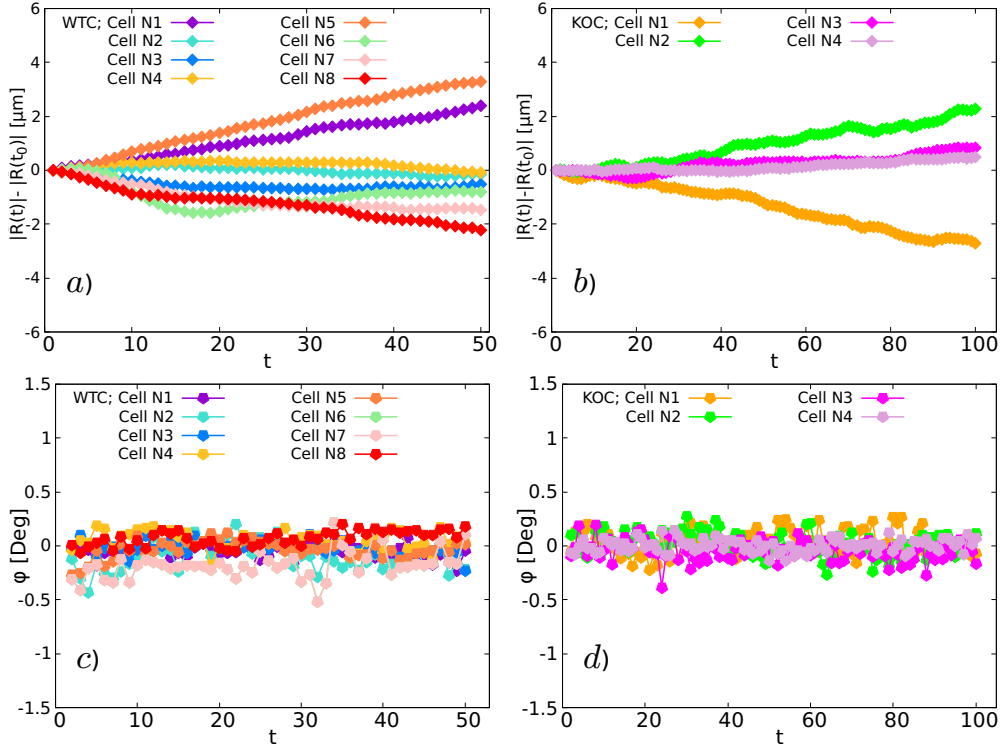


FIG. 1. Translational and rotational drift versus time for telomeres in WT and KO cells, before detrending procedure. *a)* For WT cells and total measurement time  $t = 50 * \Delta$ , relative magnitude of the drift vector  $|\vec{R}(t)| - |\vec{R}(t_0)|$  versus time. *b)* The same as in *a)* for KO cells and  $t = 100 * \Delta$ . *c-d)* Corresponding rotational drift in degrees versus time for WT and KO cells respectively. The time is measured as  $t = n * \Delta$ , with  $n = [1, 50]$  or  $n = [1, 100]$ .

To inspect the behavior of the rotation of the cell, for all the trajectories inside a given nucleus, we computed at each time frame the average rotation:  $\phi(t_i) = \sum_{j=1}^M \theta^j(t_i, \Delta t) / M$ , with  $\theta^j(t_i, \Delta t)$  the relative angle between successive vectors defined by Eq. (2). Here  $\phi(t_i)$  indicates at each time frame the average rotation around the center of mass of all telomeres in the cell. Fig. 1 *c-d)* shows the rotation angle along the trajectory for few cells in both WT and KO cells. As one can see, the rotation is very small in most of the cases.

Given these rather smooth/stable drift and small rotation angles, the drift subtraction and rotation correction procedures that we used are completely justified as one can find for other similar experimental set-ups [14]. A complete detail of our techniques are described

in the Materials and Methods section and in the SM.

### Tracking telomeres in the nucleus cell

We tracked simultaneously fluorescently tagged telomeres in WT and KO MEF cell lines, for a total measurement time of either  $T = 925$  sec or 1850 sec, see Materials and Methods for details. Typical telomere trajectories are shown in Fig. 2 for WT and KO cells. As mentioned above, while in WT cells telomeres are mainly confined in regions of typical length  $\sim 100 - 200$  nm, in KO cells telomeres cover significantly larger distances up to  $\sim 3\mu\text{m}$ . Strikingly, we note that in KO cells, the diffusion not only spans a significantly larger volume, but one can notice that there are time-windows in which the motion is highly directional (Fig. 2 *b*). This variation in the directional dynamics, either caging with no preferential direction in WT cells or unidirectional motion in KO cells, can be attributed to the respective differences in the nuclear structure of each type of cells. It was lately found that the dynamics of gene

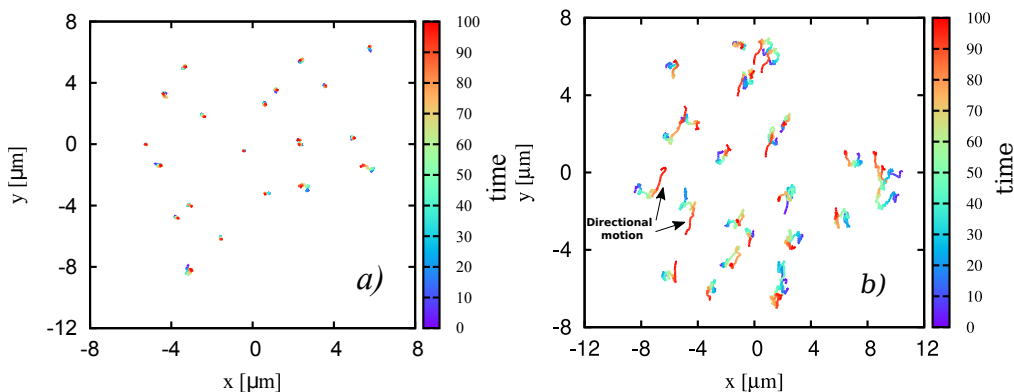


FIG. 2. Trajectories of telomeres in the nucleus. *a*) Wild type (WT) cells. *b*) Cells depleted of lamin A (KO). Telomeres moving in cells depleted of Lamin-A cover larger distances compared with telomeres diffusing in WT cells, and directional motion often occurs. The color gradient represents time measured as  $t = n * \Delta$  with  $n = [1, 100]$ . See Fig. S4 in SM for a detailed description of telomere tracks in WT cells.

loci in WT cells is sub-diffusive, and it can turn into normal-like diffusion in KO cells [4]. It was suggested [4] that Lamin-A forms intra and inter-chromosomal cross-links of DNA, thereby turning the free long chromosome polymer into a gel-like structure, which naturally exhibits highly restricted dynamics in space and time. Moreover, it was shown that by

transfecting Lamin-A back to these cells, the sub-diffusive nature of the chromatin dynamics is reestablished. It demonstrates that Lamin-A is of major importance for maintaining a constrained diffusion. Hereinafter, we explain how the presence/absence of Lamin-A protein renders a different behavior in the spreading of telomere trajectories, directed single particle dynamics, and correlation between pairs of particles.

### Laplace-like PDF of the telomeres displacement

After detrending telomeres trajectories in the cell nucleus, first we analyze the dynamics of telomeres in WT and KO cells by calculating the distribution of the traced displacements over different time intervals  $\Delta t$ . The distribution of displacements for WT telomeres was previously studied in [5]. Here we ask how does Lamin-A depletion modify this distribution and show that it has a dramatic effect on the scale of the motion. However the distribution of displacements, as a stand alone does not yield insights on the coherent motion and correlations amongst telomeres, features that will be treated later.

The displacements along the  $x$  and  $y$  axes are defined as  $\Delta X = X(t + \Delta t) - X(t)$  and  $\Delta Y = Y(t + \Delta t) - Y(t)$ ; with  $t = n * \Delta$  and  $\Delta \xi = \{\Delta X, \Delta Y\}$ . Fig. 3 shows the positional PDF in semi-log scale for telomeres in WT and KO cells with  $\Delta t = 10\Delta$ , see panels *a* and *b* respectively. For both cell types we found that the positional PDF collapses to the same plot fitted by a model composed of a linear combination of Gaussian and Laplace distributions (solid lines), which is defined as

$$P(\Delta \xi) = (1 - w) \frac{e^{-\frac{\Delta \xi^2}{4\sigma^2}}}{\sqrt{4\pi\sigma^2}} + w \frac{e^{-\frac{|\Delta \xi|}{\lambda}}}{2\lambda}, \quad (1)$$

here  $\lambda$  is the decay length of the exponential tails,  $\sigma^2$  the variance of the Gaussian central part and  $w$  the weight of the Laplace distribution. The analysis of residuals shown in Fig. S6 in SM corroborates that Eq. (1) is a good model for describing telomere dynamics. We also tried to fit the data to a linear combination of two Gaussian curves. We found that the linear combination of a Gaussian and Laplace distributions gives significantly better results, see SM for details.

There are several noteworthy observations about the distributions of telomere displacement (Fig. 3). First, we note that there are few displacements in Fig. 3a) at large positive range. They correspond to only 0.15% of the total set of points and can be considered as

outliers. Secondly, note that there is a slight difference in the x and y coordinates in Fig. 3b). It results from only 3 out of 7 cells that are measured for KO cells (see Fig. S8 in SM). The nucleus of the cell is not always isotropic, so these results can occur naturally. Additionally, since cells and nuclei are non-identical objects, it is unsurprising that some of the cells are more anisotropic than others.

Packets with exponential decaying tails have been thoroughly investigated both theoretically [15–23] and experimentally [24–32]. Fig. 3 *c-d* show the distributions of the normalized displacements for  $\Delta t = \{\Delta, 10\Delta, 20\Delta\}$ . The normalization is performed by dividing the displacements  $\Delta\xi$  by the standard deviation, defined as  $\sigma_{\Delta\xi} = \sqrt{Var(\Delta\xi)}$ . As one can see in both cell types and for all  $\Delta t$ , the PDF is well described by Eq. (1) (black solid line). For comparison in each case the Gaussian distribution is shown as a black dashed line, further details of the fitting parameters are shown in the SM. The striking features are the exponential tails and the larger spread of the KO case, compared to the WT case (Fig. 3 *a -b*).

Independently of the level of Lamin-A in the nucleus, the short displacements of the telomeres are described by Gaussian statistics and for large displacements the distribution has exponential tails, which coincides with the behavior of the Laplace distribution. A strong effect on the spreading of the displacements of telomeres was found when Lamin-A is completely depleted. From the fitting of Eq. (1) to experimental data, the decay length obtained by the corresponding fitting, was  $\lambda \sim 0.4 \mu m$  for telomeres in KO cells when  $\Delta t = 20\Delta$ , which is four times larger compared with WT cells,  $\lambda \sim 0.1 \mu m$ . The average total displacement  $\langle |\Delta\xi| \rangle = \langle |\xi(T) - \xi(0)| \rangle$ , behaves similarly with  $\langle |\Delta X| \rangle \sim 0.5 \mu m$  and  $\langle |\Delta Y| \rangle \sim 0.6 \mu m$  for telomeres in KO cells compared to  $\langle |\Delta X| \rangle \sim 0.15 \mu m$  and  $\langle |\Delta Y| \rangle \sim 0.15 \mu m$  for telomeres in WT cells. Despite this difference in the spreading, for both cases we found that the decay length  $\lambda$  in Eq. (1) grows as the square root of  $\Delta t$ , *i.e.*  $\lambda \propto \sqrt{\Delta t}$ , which is consistent with a linear MSD (see Fig. S5 and Fig. S9 in SM). This dependence of  $\lambda$  was also found in other heterogeneous systems [25, 33–35].

The information gained from Fig. 3 is naturally an averaged quantity, namely one cannot pinpoint the origin of the exponential decaying tails, *i.e.* Laplace diffusion [36]. Does it appear because different telomeres exhibit distinct types of motion? Or is each trajectory heterogeneous, which means that there is an interplay of fast and slow motion? Fig. 3 suggests that the Gaussian part of the PDF is associated with a slow dynamics phase (for



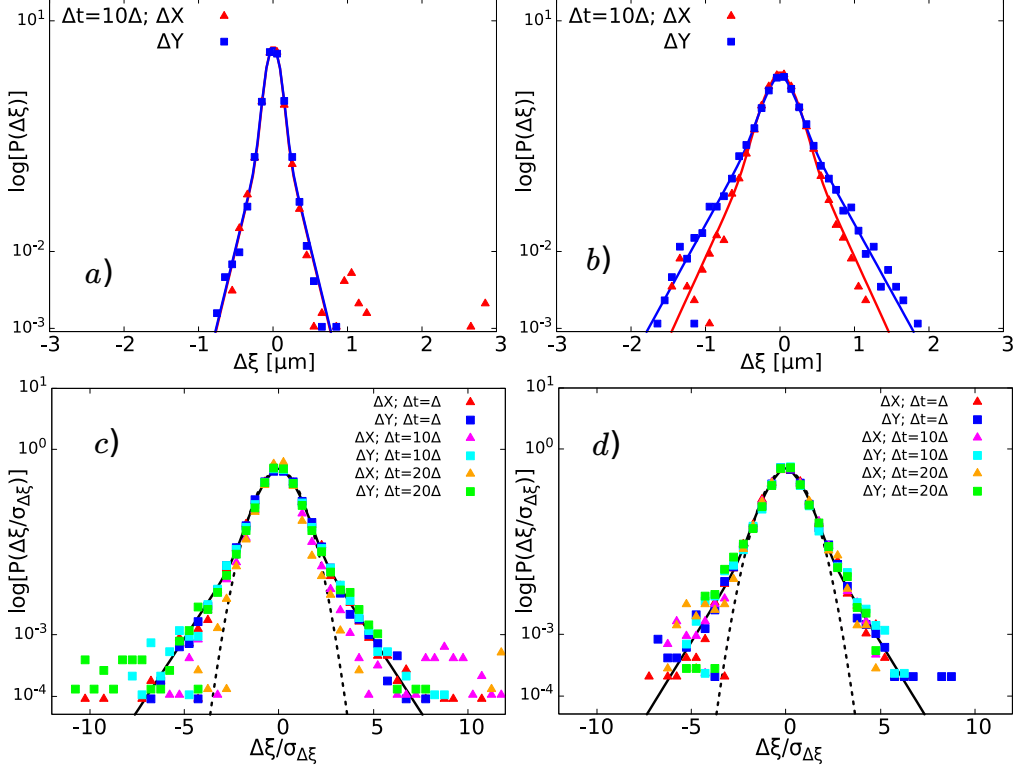


FIG. 3. Distribution of telomere displacements  $\Delta\xi = \{\Delta X, \Delta Y\}$  (red triangles and blue squares in correspondence) WT *a*) and KO *b*) cells, with  $\Delta t = 10\Delta$ . **c-d**) Same data for normalized displacements  $\Delta\xi/\sigma_{\Delta\xi}$ , for WT and KO cells respectively for  $\Delta t = \{\Delta, 10\Delta, 20\Delta\}$ , and X-Y directions (colored triangles x-coordinate and colored squares y-coordinate). Here  $\sigma_{\Delta\xi}$  is the respective standard deviation. For comparison in each case Gaussian statistics is shown in black dashed lines. In all cases for any time scale,  $\Delta\xi$  and cell type the positional PDF collapses into the same plot given by the model of a superposition of a Gaussian center and exponential tails Eq. (1) (solid lines). Nonetheless, the spreading of the positional PDF is larger for telomeres in KO cells compared with WT cells.

short distances), while the Laplace exponential decay is associated with fast motion (for long distances). In the section Model, we show how these slow and fast phases are related to caging, pure diffusion and directed motion.

## Caged and Directed motion of telomeres inside the nucleus

The positional PDF shown above emphasizes the spatial and temporal scales of telomeres in the nuclei of WT and KO cells, but the directional trajectories that only appear in short time-windows are averaged out. In order to expose its nature, we use a statistical tool that calculates the relative angle between each two points along the particle trajectory separated by  $\Delta t$ . Namely the absolute value of the turning angle which is denoted by  $\theta(t; \Delta t)$  [37–41], see inset in Fig. 4 *a*. The relative angle for any  $\Delta t$  is defined as:

$$\cos \theta(t, \Delta t) = \frac{\Delta \vec{X}(t; \Delta t) \cdot \Delta \vec{X}(t + \Delta t; \Delta t)}{\|\Delta \vec{X}(t; \Delta t)\| \|\Delta \vec{X}(t + \Delta t; \Delta t)\|}, \quad (2)$$

with the vector displacements  $\Delta \vec{X}(t; \Delta t) = (X(t + \Delta t) - X(t), Y(t + \Delta t) - Y(t))$  and  $\|\cdot\|$  the Euclidean norm.

We compute for each  $t$  the relative angle between successive displacements within different lapse-times  $\Delta t = \{\Delta, 5\Delta, 10\Delta, 20\Delta\}$  and calculate the respective distribution of the relative angle. In persistent trajectories a particle tends to move in the same direction, exhibiting small values of  $\theta(t; \Delta t)$ . On the other hand, in anti-persistent tracks a particle flips its direction of movement, remaining caged, and  $\theta(t; \Delta t)$  has values close to  $\pi$  [37, 42, 43].

Fig. 4 *a* shows the relative angle distribution for telomeres in WT cells, as a function of the normalized variable  $\theta/\pi$ . We see that for any time scale, the relative angle distribution has a peak at  $\pi$  and hence the displacements are negatively correlated, see the autocorrelation function of the displacements in Fig. S10 *a-b* in SM. Therefore the process is anti-persistent, implying caged dynamics [37, 42, 43].

In contrast, for KO cells  $P(\theta)$  has a maximum at  $\theta = 0$  for and  $\Delta t$  studied, see Fig. 4 *b*. This implies that the motion is now directed for  $\Delta t \leq 20\Delta$ . This persistent behavior in telomeres moving in KO cells is translated into trajectories like those displayed in Fig. 2 *b*, where telomeres tend to continue in the same direction for a significant time window.

There is a striking difference between the behavior of  $P(\theta)$  for both WT and KO cells (Fig. 4) and the case of regular Brownian motion, *e.g.* a random walk. For Brownian dynamics the distribution of the relative angle is uniform in the whole range of  $\theta$ , irrespective of  $\Delta t$  [37, 43]. Indeed, every movement is uncorrelated with the previous one, so every direction is equally probable (for any time scale). The non-uniform profiles of  $P(\theta)$  for the

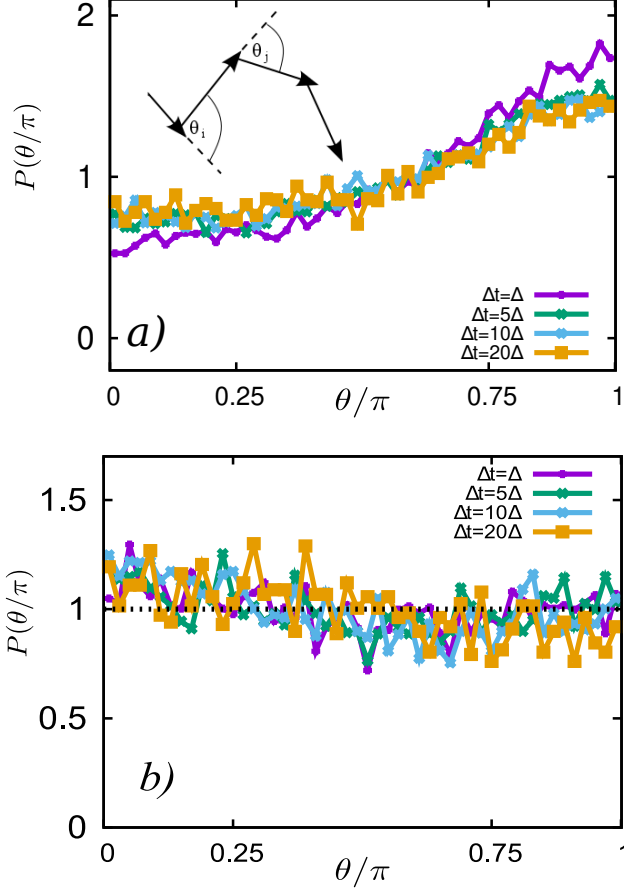


FIG. 4. Probability distribution of the deflection angle along telomeres trajectories as a function of the normalized angle  $\theta/\pi$  for few different lag-times  $\Delta t = \{\Delta, 5\Delta, 10\Delta, 20\Delta\}$ . *a)* WT cells, the distribution mode is at  $\theta = \pi$ , indicating anti-persistent diffusion. Inset: examples of relative angles  $\theta_i, \theta_j$  defined by Eq.(2). *b)* KO cells, the distribution mode is at  $\theta = 0$  indicating the presence of directed motion. The black dashed line, represents the corresponding angular distribution for a random walk (a uniform distribution).

WT and KO configurations reveal the temporal structure of the motion. For the KO case within time scales of  $t \lesssim 300$  sec, the motion is directed as the particle has a preference to travel in the previously explored direction. On the other hand, WT dynamics shows the presence of caging at any time scale (a peak for the relative angle distribution at  $\theta = \pi$ , see Fig. 4 *a)*).

The difference between caging and directed motion, becomes even clearer when we observe the evolution of the average relative angle as a function of the sampling time (Fig. 5). For trajectories of telomeres in WT cells, the *ensemble* average relative angle ( $\langle\theta(t, \Delta t)\rangle/\pi$ ) and

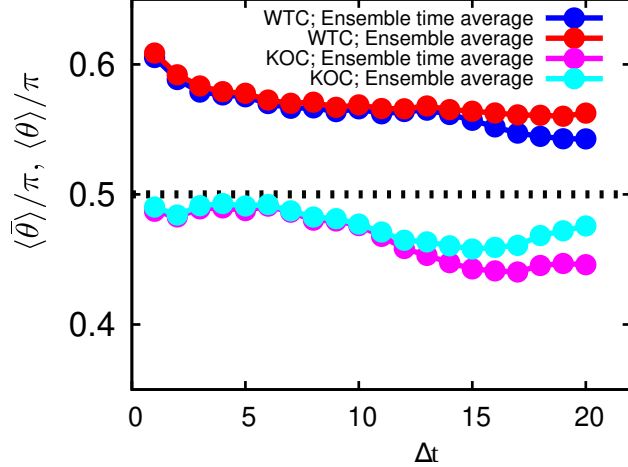


FIG. 5. *Ensemble* average relative angle ( $\langle \theta(t, \Delta t) \rangle / \pi$ ) and *ensemble* time average relative angle per trajectory  $\langle \bar{\theta}(t, \Delta t) \rangle / \pi$  as a function of  $\Delta t = n\Delta$  with  $\Delta = 18.5\text{s}$  and  $n = [1, 20]$ . For WT cells the *ensemble* average (red circles) and the *ensemble* time average (blue circles) for all  $\Delta t$  are above the corresponding values of a random walk, *i.e.* 0.5 (black dashed line), indicating dominance of anti-persistent motion or caging. For KO cells the *ensemble* average (cyan circles) and the *ensemble* time average per trajectories (magenta circles) for any  $\Delta t$  are below 0.5, which implies presence of persistent behavior for any time scale  $\Delta t < 20\Delta$ .

the *ensemble* time average of the relative angle ( $\langle \bar{\theta}(\Delta t) \rangle / \pi$ ) are displayed in red circles and blue circles respectively. For tracks in KO cells, the respective averages are shown in cyan and magenta circles, the black dashed line indicates the average relative angle corresponding to a random walk, *i.e.*  $\langle \theta(t, \Delta t) \rangle / \pi = 0.5$ . Following results shown in Fig. 4, in WT cells we observe caging dynamics for all measurement times. We observe a reduction of the average relative angle of 10% from the short-time gap value to the long-time gap. For KO cells the average relative angles are always less compared with the random walk reference value achieving a reduction of 8%, implying an increase in persistent motion along trajectories. The minimum of the average relative angle is attained at  $\Delta t = 15\Delta \sim 270$  sec.

The relative angle statistics provides strong evidence for the existence of mechanisms that trigger both caged and directed motion inside the cell nucleus, and this difference in the dynamics depends on the presence/absence of Lamin-A protein. Next we study how these directional dynamics are correlated on pair of telomeres in WT and KO cells.

### Pair correlation for telomere dynamics

We now focus on the correlated motion of pairs of telomeres, and show that the motion cannot be considered as mutually independent. In other words we search for the spatial correlation length; a scale on which dynamics is correlated. We compute the pair correlation of telomeres as follows: for a pair of telomere tracks labeled as telomere  $A$  and telomere  $B$ , in the same nucleus, we measure the initial separating distance  $d_{AB} = \sqrt{(x^A(t_1) - x^B(t_1))^2 + (y^A(t_1) - y^B(t_1))^2}$ . We then compute the correlation function:

$$\beta_{A,B}(\Delta t, d_{AB}) = \frac{1}{N} \sum_{n=1}^N \Delta \hat{X}_A(t_n, \Delta t) \cdot \Delta \hat{X}_B(t_n, \Delta t), \quad (3)$$

with  $N$  the number of sampling points in each trajectory,  $t_n = n * \Delta$ ,  $\Delta \hat{X}_A(t_n, \Delta t) = \overline{\Delta \vec{X}_A(t_n, \Delta t)} / \|\overline{\Delta \vec{X}_A(t_n, \Delta t)}\|$ , where  $\overline{\Delta \vec{X}_A(t_n, \Delta t)} = \vec{X}_A(t_n + \Delta t) - \vec{X}_A(t_n)$  and  $\vec{X}_A(t_n) = (x^A(t_n), y^A(t_n))$ . We compute the *ensemble* average  $\langle \cdot \rangle$  of Eq. (3) per cell type and bins for different values of  $d_{AB}$  (see details in SM). Then, for a fixed value of  $d_{AB}$ , the average per cell type (WT or KO) is performed. For uncorrelated random walkers the pair correlation has zero values for any  $d_{AB}$  and  $\Delta t$ , as shown in Fig. S12 in SM.

Fig. 6 presents the pair-correlation of telomeres for different time-scales (Eq. (3)) as a function of the initial spreading distance between them. As one can see, in Fig. 6 for both cell types when telomeres are initially close to one another, the pair correlation is positive which means that they move coherently in the same direction. This effect is clearly more pronounced for KO cells, where the pair correlation exhibited significant positive values, for which the maximum attained is at 0.38. Particularly telomeres in WT cells exhibit regions of  $\sim 1\mu\text{m}$  in extent where the pair correlations are positive, see Fig. 6 *a*. For KO cells the extent of positive correlations is  $\sim 4\mu\text{m}$ , see Fig. 6 *b*. Interestingly, in both cell types when telomeres are far away from each other inside the same cell, they move coherently in the opposite direction. Remarkably we found that irrespectively the presence of Lamin-A, these pair correlations exhibit the same shape in both cell types, but the correlation level is different. Given the above observations, we developed a physical model for telomeres dynamics that can explain these results, paying specific attention to the caging and directed motion dynamics.

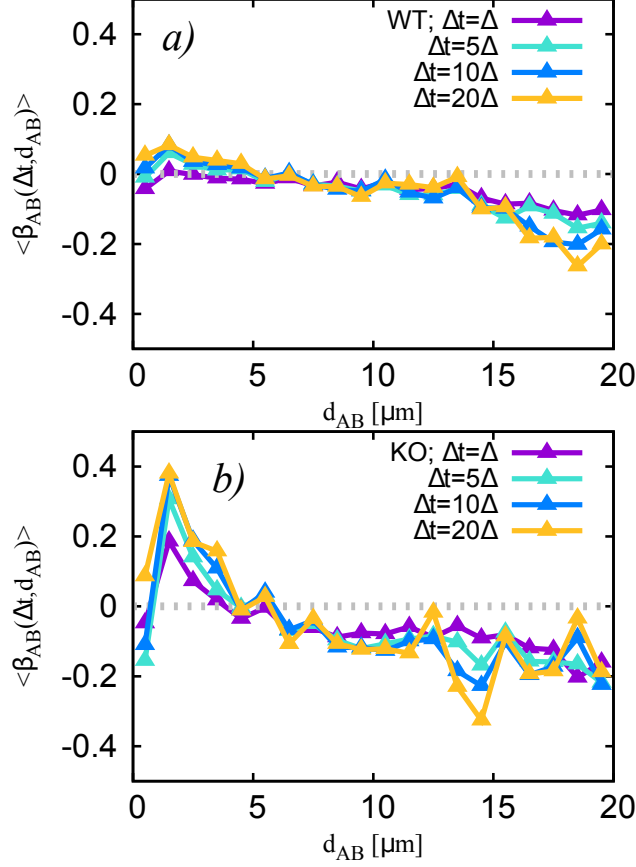


FIG. 6. Pair correlation of telomeres as a function of their initial separating distance. *a)*: For telomeres diffusing in WT cells, corresponding *ensemble* average of the pair correlation of telomeres defined by Eq. (3), for different measurement times  $\Delta t = \{\Delta, 5\Delta, 10\Delta, 20\Delta\}$  (color triangles). *b)*: The same as above but for telomeres in KO cells. For WT cells there are very small positive correlations of  $\sim 0.05$  at a separation distance of  $\sim 1.4\mu m$  (for all time-scales) and a small negative correlation of  $\sim 0.2$  for large distances. For KO cells the pair correlation exhibits large positive values (maximum of 0.38) at short telomere distances of  $\sim 1.4\mu m$ , and a significant negative correlation of  $-0.25$  at larger distances. This indicates that for both cell types the same correlation pattern appears. Nevertheless, it is significantly more pronounced in KO cells relative to WT cells.

## Model

Based on the experimental data of telomere dynamics in WT and KO cells, we developed a physical model that fits the main features exhibited by experimental data, like the exponential decay in the distribution of displacements and the relative angle distributions. All the parameters employed in our model are obtained from experimental data except for

a few free parameters dealing with the width of the fluctuations of the angular increments.

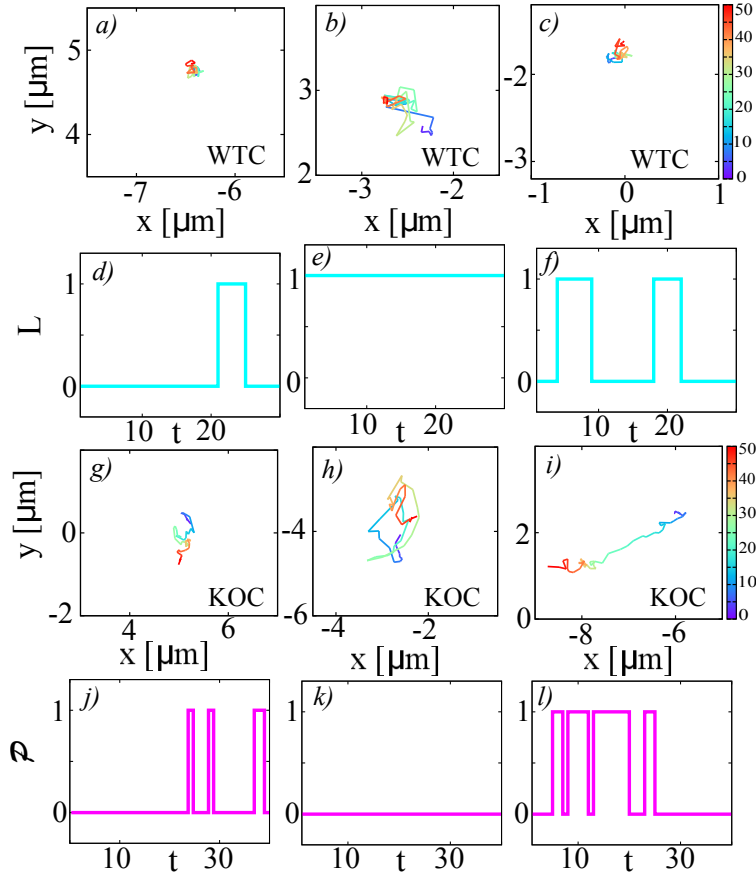


FIG. 7. Representative time series, with predominantly small jumps *a)*, large jumps *b)* and switching between small and large jumps *c)* of telomeres in WT cells. In *d)*-*f)* we show the corresponding two state series representation of the length size jumps  $L(t, \Delta t) = \{0, 1\}$  (cyan solid lines). For telomeres in KO cells we show representative tracks with predominantly non-persistent dynamics *g)*-*h)* and persistent one *i)*. The corresponding two state series representation of the level of persistence  $\mathcal{P}(t, \Delta t) = \{0, 1\}$  are shown in *j)*-*l)* (magenta solid lines). The color gradient represents time as  $t = n * \Delta$  with  $n = [1, 50]$ . We employed for the two state analysis  $\Delta = 10\Delta$  for WT cells and  $\Delta = 5\Delta$  for KO ones.

As reported in many single particle tracking experiments we see a wide fluctuation in behaviors of individual molecules [44, 45]. For instance for telomeres in WT cells we found intermittency between caged and diffusive intervals, see Fig. 7 *a-f)*. This was deduced by computing the local convex hull (LCH) at each time frame and given a specific time window, see Fig.8 and Material and Methods. Specifically at each time frame for the respective LCH

we obtain the average largest diameter labeled as  $\langle \mathcal{D}_{max} \rangle$ . Then we define a criterion for discriminating between the “large jumps” or diffusive phase and “small jumps” or caged phase as following: If  $\mathcal{D}_{max}(t, \Delta t) > \langle \mathcal{D}_{max} \rangle$  the LCH contains “large jumps” (and its labeled as  $L(t, \Delta t) = 1$  ). In other case,  $\mathcal{D}_{max}(t, \Delta t) < \langle \mathcal{D}_{max} \rangle$ , the LCH contains “small jumps” (calling  $L(t, \Delta t) = 0$ ). Thus we generate a dichotomous process  $L(t, \Delta t) = \{0, 1\}$  see cyan lines in Fig. 7 *d-f*). For telomeres in KO cells using a critical value for the relative angle at each time frame and within a specific time interval, we developed a similar decomposition of trajectories between persistent ( $\mathcal{P}(t, \Delta t) = 1$ ) and non-persistent intervals ( $\mathcal{P}(t, \Delta t) = 0$ ), see magenta lines in Fig. 7 *j-l*) and details in Materials and Methods.

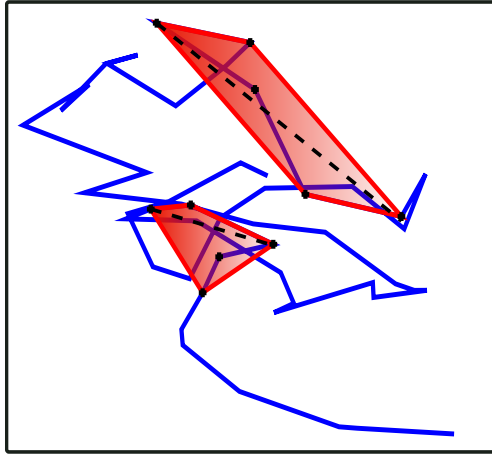


FIG. 8. Schematic representation of the LCH (red polygons) for a typical telomere trajectory (blue line). Typical LCH areas and maximum diameters are shown in red color and black dashed line respectively.

Therefore, for the dynamics of telomeres in WT cells, we suggest a modified Pearson random walk model. Recall that for a Pearson random walk [46] at each time step, a random angle is chosen on the 2D plane and then the walker advances a distance  $r$  on a straight line. Accordingly we assume a two-state model of caging and pure diffusion, where intermittent switching occurs. During caging, the Pearson random walk is assumed in a circular cage of radius  $r_c$  with reflecting boundary conditions. For the pure diffusive phase  $r_c \rightarrow \infty$ . We also employ different displacement lengths during different phases, namely  $r_S < r_L$ , with  $r_S$  the displacement during caging and  $r_L$  during pure diffusion. The duration of each of the two phases is randomly selected from an exponential distributions that are determined from the experimental data, see Fig. S13 of the SM. The complete algorithm is presented in Materials and Methods .



Fig. 9 demonstrates a comparison of the experimental (Figs.3, 4) and our simulation results (black triangles and gray squares). Fig. 9 *a,b* shows the comparison the displacements and relative angle in WT cells. The agreement between theory and experiment is excellent for all the observed data. The simulation data precisely follows the Gaussian distribution at short displacement and Laplace tails for larger ones Eq. (1). It also nicely follows the angular distribution data for all lag-times. Remaining statistics are displayed in Fig. S15 in SM.

As explained before, previous works demonstrated the lack of chromatin cross links, which leads to directed dynamics for  $\Delta t \leq 20\Delta$ . And as we show in Fig. 7, in KO cells we found that telomere trajectories display a switching between non-persistent and persistent intervals. Given this our model assumes intermittency between pure diffusion and directed dynamics. Therefore in the KO case the theory presents a two state model with a regular Pearson random walk and varying persistent motion. Our model works as follows. Initially, for each track we draw a random value for  $\theta_{int}$  from a uniform distribution  $U(0, 2\pi)$ . We then build the trajectory with the first step equal to  $(x_1, y_1) = (r \cos \theta_{int}, r \sin \theta_{int})$  and each following step equal to  $(x_j, y_j) = (x_{j-1} + r \cos \tilde{\theta}_j, y_{j-1} + r \sin \tilde{\theta}_j)$ . Here  $\tilde{\theta}_j = \tilde{\theta}_{j-1} + \tilde{\Delta}\theta_j$ , where  $\Delta\theta_j$  defines the level of persistence, and it is drawn at each step from a uniform distribution  $\tilde{\Delta}\theta_j \sim U(-\theta_c, \theta_c)$ . Finally, a new  $\theta_{int}$  is drawn again after  $20\Delta$  sec, see further details in Materials and Methods . By introducing  $\theta_{int}$  at the beginning of each persistent phase, we correlate the direction of successive segments of the trajectory. This is done during time scales less than  $20\Delta$ , after this time a new  $\theta_{int}$  is drawn and it is correlated in the successive segments during the same lapse of time.

We have the representative segments of trajectories, for instance: by correlating directed stages as above,  $\theta_c \rightarrow 0$  implies alternating between straight lines and random walk paths, rendering persistent segments during a time scale of  $20\Delta$ . And on the other hand, when  $\theta_c \geq \pi/2$  we have random walk behavior along the corresponding segments of the trajectories. The distribution of displacements and one of the relative angles obtained from simulated trajectories are shown in grey squares and black triangles in Fig. 9 *c* and *d* respectively. We find a good agreement with those obtained from experimental data. A Gaussian bulk with exponential decaying tails for  $P(\Delta\xi)$  and a zero peaked angular distribution are recovered, see further statistics in Fig. S17 in SM.

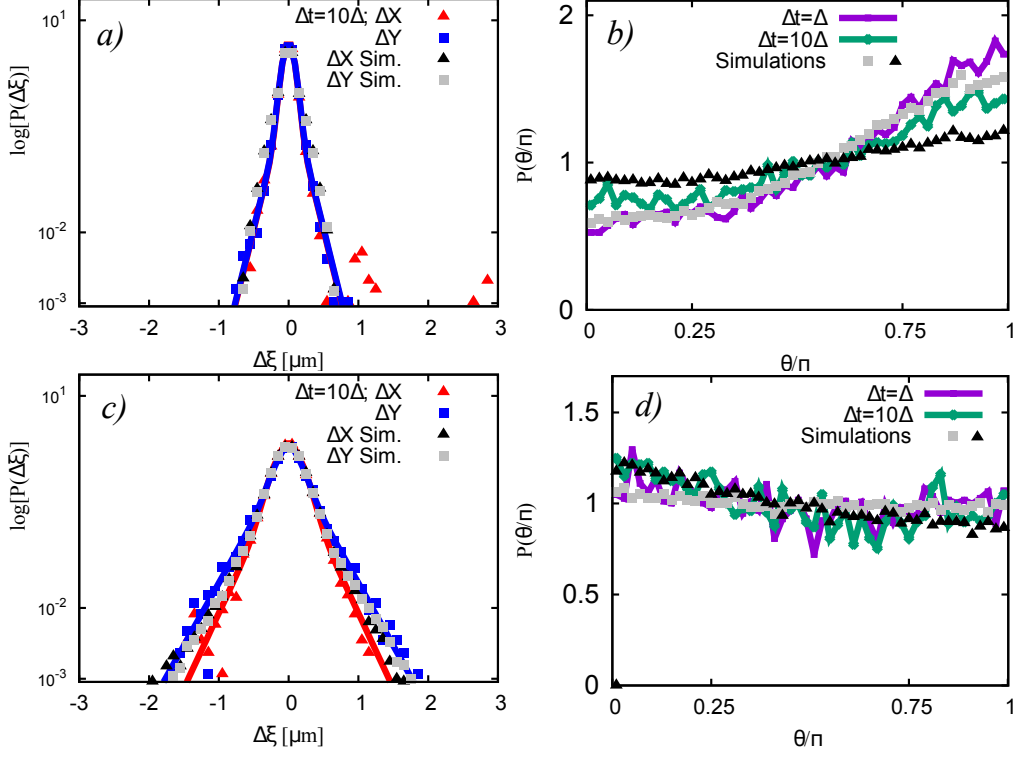


FIG. 9. Comparison between experimental data of telomeres in WT and KO cells with simulations. *a)* For telomeres in WT cells and simulation data of a two state model with caging and diffusive motion, distribution of displacements  $\Delta\xi = \{\Delta X, \Delta Y\}$  with  $\Delta t = 10$ . Experimental data is shown in red triangles and blue squares and simulation data in black triangles and grey squares respectively. *b)* For telomeres in WT cells and simulation data of a two state model with caging and pure diffusive motion, relative angle distribution experimental data in color lines and simulation data in grey squares ( $\Delta t = \Delta$ ) and black triangles ( $\Delta t = 10\Delta$ ). *c)* and *d)* the same as in *a)* and *b)* but for telomeres in KO cells and simulation data from a two state model with Pearson and varying persistence random walks. The parameters used in the simulations are specified in Materials and Methods .

## DISCUSSION

By following the details of the dynamics along single telomere trajectories, major insights were exposed. First, we identified a two-state behavior in both cell types WT and KO. In WT cells, the trajectories switch between caged and Brownian normal diffusion, while in KO cells they switch between pure diffusion and directed motion. Second, we found that in both cell types the dynamics lead to Gaussian statistics for small displacements and Laplace

(exponential tails) statistics at large displacements. Our analysis revealed that the Gaussian statistics result from caging in WT cells and free diffusion in KO cells. Additionally, the Laplace tails results from the large displacements of the free diffusion in the WT cells and by the directed motion in KO cells. Thirdly, we note that when the dynamics of WT and KO cells is compared, it is clear that the directional motion observed in KO cells is suppressed by the effect of Lamin-A in WT cells. It also explains the difference in the large spatial spread of the motion in KO cells versus small spread in WT cells.

Interestingly for trajectories in KO cells, we found persistent dynamics for times scales  $\Delta t < 20\Delta \sim 370$  sec. For this case, if after each switching between the phases the telomere “forgets” the directionality of the previously visited directed stage, the observed directionality is expected to disappear, in the sense that a uniform distribution of the relative angle describes such dynamics. Instead, the observed behavior of the relative angle PDF shows that the direction is persistent. Furthermore, we revealed that this persistent motion is connected to pair wise correlations of telomeres, Fig. 6 *b*. This suggests, that the directionality field in the nucleus of the cell when Lamin-A is absent, is patchy, in the sense that different micro regions impose quenched directionality of the motion. We may speculate that the correlated directed motion we found, is related to chromatin territory [6, 47–51], or to the vicinity of the chromatin loci to the boundaries of the cell, or possibly to spatial domains with high concentration of activity, possibly ATP driven [52], issues that must be studied later.

We speculate that the observed structure of directional correlations (Fig. 6) may be the product of the contraction or expansion of the nucleus during the different stages of the cell cycle. A similar idea was proposed in [3], in the context of long-range anisotropy-enhanced parallel diffusion of centromeres and telomeres. The short distances scale dynamics is most likely related to the coherent motion of chromatin loci found in [7] using DCS technique. The two works show that active forces are correlated on scales of micrometers.

The exponential decay of the PDF in the displacements of telomeres that was observed in this study and in [5], has also been observed in a several number of systems from glassy systems [15] to diffusion of molecules within living cells [24–31] and tracers in colloidal suspensions [53–57]. Laplace diffusion has been theoretically modelled, by diffusing diffusivity models [16, 17, 19–23], spatial quenched disorder [58–61], and interacting particle approaches [62–65]. It was shown that Laplace exponential statistics for the decay of posi-

tional PDF attains similar universal features as the Gaussian behavior of the PDF for the central part of the distribution [18, 66]. In this study, we showed for KO cells (via numerical simulations) that a correlated run and tumble model also leads to Laplace exponential decay. Nevertheless, the usual run and tumble models [67–69], as they traditionally have been developed for explaining the dynamics of bacteria, lack the long time correlations along trajectories that we have employed.

Directional dynamics appears not only for run and tumble models [67–69], but also for active Brownian particles [70–72] and Lévy walks [73–77]. The majority of these models do not establish intrinsic directionality as a mechanism of active motion, as we suggest here for telomeres in KO cells. Another popular approach to model active matter utilizes Langevin equations with active noises [78, 79]. The absence of spatial correlations (for the noise) in these models make them insufficient as a framework for our experimental system. Interestingly in [80] the emergence of long-ranged active dynamics has been linked with the presence of disordered landscapes, where the concentration of active matter is non-uniform, in some cases fractal. Our results for KO cells are in agreement with the latter idea since we saw that the inherent directionality of telomeres tracks is quenched, and temporally correlated for hundreds of seconds.

## SUMMARY

Our study focuses on several aspects of the dynamics of telomeres, for WT and KO cells. In both cases we observe that the spreading of packets of particles is not described by Gaussian statistics, but rather by Laplace-like exponential tails. As well known exponential tails decay slowly compared to Gaussian tails, however this observation as a stand alone does not lead to a direct insight with respect to coherence and persistence. A dramatic increase in the magnitude of displacements is found for the KO cells. This is related to the fact that KO cells malfunction. The motion of single particles exhibits a combination of Brownian and trapping/directed motion. The directed motion in KO cells is a clear indication for persistence and correlation between micro displacements along the paths of individual particles. This is accompanied with pair wise correlations between pair of particles, indicating coherent motion of *single molecules* in the cell nucleus, which as far as we know is the first observation of such a phenomenon. The level of directional motion crucially depends on

Lamin-A's presence. In contrast, the Laplace spreading of the telomeres dynamics and the overall structure of the pairwise correlation function does not depend on Lamin-A.

Unexpectedly, when we study the directional correlations of pairs of telomeres inside the same cell, we observe that there is a general structure for such correlations in WT and KO cells, *i.e.* positive correlations for short distances between telomeres and negative values for large distances (Fig. 6). The latter is important because independently of the presence of Lamin-A, it suggests the existence of long-ranged forces that create this coherent motion in the nucleus. Determining the origin of such forces is set up as an open question.

## MATERIALS AND METHODS

### ANALYSIS OF TRAJECTORIES

We perform SPT analysis of fluorescently labeled telomeres in WT cells, where 363 trajectories of telomeres were analyzed, 270 tracks with  $\Delta t = 50\Delta = 925$  sec and 93 with  $\Delta t = 100\Delta = 1850$  sec. In the case of telomeres in KO cells, 128 trajectories were analyzed, 59 tracks with  $\Delta t = 50\Delta = 925$  sec and 69 with  $\Delta t = 100\Delta = 1850$  sec. Particularly for WT cells and measurement time  $T = 50\Delta$ , we employed 8 different cells and on each one we tracked the following numbers of trajectories: cell #1 25 tracks, cell #2 35 tracks, cell #3 38 tracks, cell #4 25 tracks, cell #5 35 tracks, cell #6 48 tracks, cell #7 25 tracks, and cell #8 39 tracks ( with a total of 270 trajectories). For WT cells and  $T = 100\Delta$ , we employed 5 different cells for which we trace: cell #1 21 tracks, cell #2 24 tracks, cell #3 20 tracks, cell #4 13 tracks, and cell #5 15 tracks (with a total of 93 trajectories). In the case of KO cells and measurement time  $T = 50\Delta$ , we used 3 different cells each one following: cell #1 19 tracks, cell #2 17 tracks, cell #3 23 tracks (with a total of 59 trajectories) . And finally for KO cells and  $T = 100\Delta$ , we employed 4 different cells with: cell #1 18 tracks, cell #2 26 tracks, cell #3 10 tracks, and cell #4 15 tracks (with a total of 69 trajectories).

In all cases a lag time of  $\Delta = 18.5$  sec was employed, and after performing the respective SPT, a nucleus drift and rotation correction were applied. For the correction of the nucleus drift, per cell at each multiple of the lag time  $t_i = i * \Delta$ , the center of mass of each coordinate was computed:  $\langle x(t_i) \rangle = \sum_{j=1}^M x^j(t_i)/M$ ,  $\langle y(t_i) \rangle = \sum_{j=1}^M y^j(t_i)/M$ ,  $\langle z(t_i) \rangle = \sum_{j=1}^M z^j(t_i)/M$  (where M is the number of telomeres in the nucleus). Thereafter each center

of mass was subtracted forward in time (for  $t_k > t_i$  with  $k > i$ ) to the corresponding coordinate:  $x^{j*}(t_k) = x^j(t_k) - \langle x(t_i) \rangle$ ,  $y^{j*}(t_k) = y^j(t_k) - \langle y(t_i) \rangle$  and  $z^{j*}(t_k) = z^j(t_k) - \langle z(t_i) \rangle$ . Next the nucleus rotation correction was performed as follows: per cell and for all the tracks inside at each frame of time we follow: when  $i = 1$  (the first frame of time) we compute  $r_d = \sqrt{(x^{j*}(t_1))^2 + (y^{j*}(t_1))^2}$  and  $\theta^j(t_1) = \text{acos}(x^{j*}(t_1)/r_d)$ , if  $y^{j*}(t_1) < 0$ , we make  $\theta^j(t_1) = -\theta^j(t_1)$ . Then we compute the average as  $\langle \theta(t_1) \rangle = \sum_{j=1}^M \theta^j(t_1)/M$ . When  $i > 1$ , we compute  $r_1 = \sqrt{(x^{j*}(t_i))^2 + (y^{j*}(t_i))^2}$  and  $r_2 = \sqrt{(x^{j*}(t_{i-1}))^2 + (y^{j*}(t_{i-1}))^2}$ . With  $\theta^j(t_i) = \text{acos}((x^{j*}(t_i) * x^{j*}(t_{i-1}) + y^{j*}(t_i) * y^{j*}(t_{i-1})) / (r_1 r_2))$  and if  $\text{asin}((-x^{j*}(t_i) * y^{j*}(t_{i-1}) + y^{j*}(t_i) * x^{j*}(t_{i-1})) / (r_1 r_2)) < 0$ , we make  $\theta^j(t_i) = -\theta^j(t_i)$ . Then the average is computed just when  $r_2 > 0.5$  (neglecting trajectories close to the origin), as  $\langle \theta(t_i) \rangle = \sum_{j=1}^M \theta^j(t_i) / \tilde{M}$ , with the number of track which satisfy this criterion. Then as above for  $t_k > t_i$  with  $k > i$ , the inverse rotation matrix was applied as:  $x^{j'}(t_k) = x^{j*}(t_k) \cos(\langle \theta^j(t_i) \rangle) + y^{j*}(t_k) \sin(\langle \theta^j(t_i) \rangle)$  and  $y^{j'}(t_k) = -x^{j*}(t_k) \sin(\langle \theta^j(t_i) \rangle) + y^{j*}(t_k) \cos(\langle \theta^j(t_i) \rangle)$ . In this way the final coordinates  $(x^{j'}(t_k), y^{j'}(t_k))$  have no trend or bias in rotation. The full algorithm is shown in SM.

## CHARACTERIZING THE TIME SERIES

*Using the relative angle time series.* To differentiate between periods of persistent and non-persistent motion on a single track in KO cells, we employed the relative angle defined by (2) at an intermediate span of time  $\Delta t = 5\Delta$  and  $\Delta t = 10\Delta$ . Thus from the time series of the telomeres without Lamin-A  $\{x(t), y(t)\}$  with  $t = n * \Delta$ , first we obtain the time series on the angle  $\{\theta(t, \Delta t)\}$ . For each time step we compare  $\theta(t, \Delta t)$  with a critical value named  $C$ . In this case  $C$  defines a threshold of the angles, letting the separation between the persistent and non-persistent motions, we define the critical relative angle as  $C = 30^\circ$  [77].

So the criterion for distinguish between persistent and non-persistent motion is the following: If  $\theta(t, \Delta t) < C$  (there is persistent motion) and we label it as  $\mathcal{P}(t, \Delta t) = 1$ . Else if  $\theta(t, \Delta t) \geq C$  (the dynamics in non-persistent) and it is labeled as  $\mathcal{P}(t, \Delta t) = 0$ . In this way we generate a two state time series which we call  $\mathcal{P}(t, \Delta t) = \{0, 1\}$  (see magenta lines in Fig. 7).

*Using local convex hull analysis.* A typical statistical tool for detecting the existence of different phases of transport with various jump sizes is the local convex hull (LCH) analysis

[29, 81]. LCH technique is described as follows. For a data set with points  $\{\vec{X}_1, \vec{X}_2, \dots, \vec{X}_m\}$  its convex hull ( $CH$ ) is the set of all convex combinations which can be made with the data points,

$$CH = \left\{ \sum_{k=1}^m \alpha_k \vec{X}_k \mid \sum_{k=1}^m \alpha_k = 1 \right\}. \quad (4)$$

In the  $2D$  case  $\vec{X} \in \mathbb{R}^2$ ,  $CH$  is the minimal convex polygon that encloses all the data points  $\{\vec{X}_1, \vec{X}_2, \dots, \vec{X}_m\}$ . For employing CH in the time series of the telomeres, we used time windows  $\Delta t = 5\Delta$ , and  $\Delta t = 10\Delta$ , such that at each  $t = n * \Delta$  we define the corresponding LCH given by (4) on the data points  $\{\vec{X}_t, \vec{X}_{t+\Delta}, \vec{X}_{t+2\Delta}, \dots, \vec{X}_{t+\Delta t}\}$ . Then for each LCH we compute the maximum diameter  $\mathcal{D}_{max}(t, \Delta t)$ , largest distance between the points  $\{\vec{X}_t, \vec{X}_{t+\Delta}, \vec{X}_{t+2\Delta}, \dots, \vec{X}_{t+\Delta t}\}$ , of the corresponding polygon, see Fig. 8. In this figure we show two typical LCH polygons (using Eq. (4) in the main text and within  $\Delta t = 5\Delta$ ) in red color solid line. Also in the same figure we show the Area  $A$  (displayed in red shaded color) and the maximum diameter (black dashed lines) of the respective LCH polygon.

## ESTIMATION OF THE WAITING TIMES

Representative examples of the two state decomposition of trajectories in terms of the level of persistence ( $\mathcal{P}(t, \Delta t)$ ) for KO cells and the relative jump size ( $L(t, \Delta t)$ ) for WT cells, is shown in Fig. 7.

In both cells types using the time series of  $\mathcal{P}(t, \Delta t)$  (magenta lines) and  $L(t, \Delta t)$  (cyan lines), we extracted the waiting times corresponding to the persistent phase and non-persistent phase, labeled as  $\tau_{\mathcal{P}}$  and  $\tau_{N\mathcal{P}}$  respectively. And the waiting times  $\tau_L$  and  $\tau_S$  for the long jump phase and the small jump one. In all cases the corresponding distributions follow a discrete exponential distribution, well fitted by the geometric distribution with mass distribution  $P(\tau) = (1 - p)^{\tau-1}p$ , with  $0 < p \leq 1$  and  $\tau = 1, 2, 3, \dots$ , (see Fig. S13 in SM). Via this classification of trajectories we obtained the mean waiting times for trajectories in WT cells,  $\langle \tau_L \rangle = 5.8\Delta < \langle \tau_S \rangle = 9.5\Delta$  using  $\Delta t = 5\Delta$ , and  $\langle \tau_L \rangle = 9.2\Delta < \langle \tau_S \rangle = 14.9\Delta$  employing  $\Delta t = 10\Delta$ . For trajectories in KO cells,  $\langle \tau_{\mathcal{P}} \rangle = 1.6\Delta < \langle \tau_{N\mathcal{P}} \rangle = 6.7\Delta$  using  $\Delta t = 5\Delta$  and  $\langle \tau_{\mathcal{P}} \rangle = 2\Delta < \langle \tau_{N\mathcal{P}} \rangle = 7.4\Delta$ .

## SIMULATION MODELS

*Two state model with caging and pure diffusion.* In this case we define two waiting times, one for the caged with small length jumps called  $\tau_S$  and other for the pure diffusive phase with larger length jumps named  $\tau_L$ . Both waiting times are sampled from the corresponding empirical distribution  $P(\tau_S)$  and  $P(\tau_L)$ , see Fig. S13 *b*. These distributions were obtained from the two state decomposition in terms of the jump size length of the trajectories and represented by the time series of  $L(t, \Delta t)$  (see Fig. 7). And both were fitted with the geometric distribution with mean values  $\langle \tau_L \rangle = 9\Delta < \langle \tau_S \rangle = 14.9\Delta$ , see SM.

We consider equilibrium initial conditions, namely with probability  $\langle \tau_S \rangle / [\langle \tau_S \rangle + \langle \tau_L \rangle]$  the particle starts from the caging phase and with probability  $\langle \tau_L \rangle / [\langle \tau_S \rangle + \langle \tau_L \rangle]$  it starts from the pure diffusive one. Then the trajectory alternates between the two phases until a final time  $T * N$ , with  $N$  the sampling time.

Particularly each phase is defined as follows. For the caging phase during a random time  $\tau_S * N$  for each sub-step we implement a Pearson random walk, with  $\tilde{\theta}_i \sim U(0, 2\pi)$  and  $(x_i, y_i) = (x_{i-1} + r_S * \cos \tilde{\theta}_i, y_{i-1} + r_S * \sin \tilde{\theta}_i)$ , and reflecting boundary conditions within a circular cage with radius  $r_c = 0.01\mu\text{m}$ . For the pure diffusive phase,  $r_c \rightarrow \infty$ , during a random time  $\tau_L * N$ , we sample  $\tilde{\theta}_i \sim U(0, 2\pi)$  and  $(x_i, y_i) = (x_{i-1} + r_L * \cos \tilde{\theta}_i, y_{i-1} + r_L * \sin \tilde{\theta}_i)$ . Notice that the displacement length depends on the phase where the particle is, they satisfy  $r_S < r_L$ .

We sample the positions along the corresponding trajectory each  $N$  sub-steps. The simulations were done using parameters close to the experimental ones. A final time of  $T = 50$ , sampling time of  $N = 20$ , displacement length in the caging phase  $r_S = 0.005\mu\text{m}$ ,  $r_L = 0.02\mu\text{m}$  in the pure diffusive phase and  $\langle \tau_S \rangle = 9\Delta < \langle \tau_L \rangle = 15\Delta$ . We employ an *ensemble* of 3000 different particles.

*Two state model with Pearson and varying persistence random walks.* Similarly as for the model defined above we define a non-persistent Pearson random walk phase with waiting times  $\tau_{NP}$  and a varying persistence phase with  $\tau_P$ . The corresponding waiting times are sampled from the distributions obtained from the two state analysis of the level of persistence, see Fig. S13 *d* in SM.

For each trajectory we draw an angle  $\theta_c \sim N(\bar{\theta}, \sigma_\theta^2)$ , with  $\bar{\theta}(t, \Delta t)$  the average relative angle and  $\sigma_\theta^2$  its respective variance. Also at the beginning  $\theta_{int} \sim U[0, 2\pi]$  is drawn. We



consider equilibrium initial conditions, namely with probability  $\langle\tau_{NP}\rangle/[\langle\tau_{NP}\rangle + \langle\tau_{\mathcal{P}}\rangle]$  the particle starts from the Pearson random walk phase and with probability  $\langle\tau_{\mathcal{P}}\rangle/[\langle\tau_{NP}\rangle + \langle\tau_{\mathcal{P}}\rangle]$  it starts from the varying persistent one. Then the trajectory alternates between the two phases until a final time  $T * N$ , with  $N$  the sampling time.

Thus for the Pearson random walk phase during a random time  $\tau_{NP} * N$  for each sub-step we do (without restrictions of motion)  $\tilde{\theta}_i \sim U(0, 2\pi)$  and  $(x_i, y_i) = (x_{i-1} + r * \cos \tilde{\theta}_i, y_{i-1} + r * \sin \tilde{\theta}_i)$ . For the varying persistent phase we proceed as follows. During a random time  $\tau_{\mathcal{P}} * N$ , for the first sup-step we make  $\tilde{\theta}_i = \theta_{int}$  and we update the positions as  $(x_i, y_i) = (r * \cos \theta_{int}, r * \sin \theta_{int})$ . Then for sub-steps  $j > i$ , we draw  $\tilde{\Delta}\theta_j \sim U(-\theta_c, \theta_c)$ , we make  $\tilde{\theta}_j = \tilde{\theta}_{j-1} + \tilde{\Delta}\theta_j$  and  $(x_j, y_j) = (x_{j-1} + r * \cos \tilde{\theta}_j, y_{j-1} + r * \sin \tilde{\theta}_j)$ . In order to avoid correlations in the varying persistence phases for time scales larger than  $20\Delta$ , at each  $20 * \Delta$ ,  $\theta_{int}$  is drawn again.

Sampling the positions along the corresponding trajectory each  $N$  sub-steps. The respective parameters employed were  $T = 50$ ,  $N = 20$ ,  $r = 0.015\mu\text{m}$ ,  $\langle\tau_{\mathcal{P}}\rangle = 2\Delta < \langle\tau_{NP}\rangle = 7\Delta$ ,  $\bar{\theta} = 1.48$ ,  $\sigma_{\bar{\theta}}^2 = 0.86$  and an *ensemble* of 3000 different particles.

### ***Code availability***

Numerical simulations of our model, computation of the relative angles, and autocorrelation functions were done employing *C* language programs. The computation of displacements, correlation coefficient, and LCH analysis were done with Octave/Matlab scripts. The fitting and computation of normalized histograms were obtained with gnuplot generic routines. All scripts are available at the GitHub repository: <https://github.com/mariohidalgosoria/Telomeres>

### ***Data availability***

All the data sets obtained experimentally, by data analysis or by numerical simulations are available from the corresponding authors upon request.

## **AUTHOR CONTRIBUTIONS**

EB, YG and SB designed the research; YG and YH performed the experiments; MHS and SB performed the data analysis; MHS performed the numerical simulations; MHS, SB, EB, and YG wrote the paper.

## CONFLICTS OF INTEREST

The authors declare no competing interests.

## ACKNOWLEDGEMENTS

The support of Israel Science Foundation Grants 1614/21 (EB and MHS) and 2796/20 (SB) is acknowledged as well as the Israel Science Foundation Grants 1902/12, 1219/17 and 2624/22 (YG and YH) and the S. Grosskopf grant for Generalized dynamic measurements in live cells at Bar Ilan University.

- 
- [1] C.-H. Chuang, A. E. Carpenter, B. Fuchsova, T. Johnson, P. de Lanerolle, and A. S. Belmont, *Curr. Biol.* **16**, 825 (2006).
  - [2] I. Bronstein, Y. Israel, E. Kepten, S. Mai, Y. Shav-Tal, E. Barkai, and Y. Garini, *Phys. Rev. Lett.* **103**, 018102 (2009).
  - [3] E. Kepten, A. Weron, I. Bronstein, K. Burnecki, and Y. Garini, *Biophys. J.* **109**, 1454 (2015).
  - [4] I. Bronshtein, E. Kepten, I. Kanter, S. Berezin, M. Lindner, A. B. Redwood, S. Mai, S. Gonzalo, R. Foisner, Y. Shav-Tal, and Y. Garini, *Nat. Commun.* **6**, 8044 (2015).
  - [5] L. Stadler and M. Weiss, *New J. Phys.* **19**, 113048 (2017).
  - [6] A. Vivante, E. Brozgol, I. Bronshtein, V. Levi, and Y. Garini, *Genes Chromosom. Cancer* **58**, 437 (2019).
  - [7] A. Zidovska, D. A. Weitz, and T. J. Mitchison, *Proc. Natl. Acad. Sci.* **110**, 15555 (2013).
  - [8] A. Vivante, I. Bronshtein, and Y. Garini, *Biophys. J.* **118**, 2258 (2020).
  - [9] W. H. De Vos, F. Houben, R. A. Hoebe, R. Hennekam, B. van Engelen, E. M. Manders, F. C. Ramaekers, J. L. Broers, and P. Van Oostveldt, *Biochim. Biophys. Acta* **1800**, 448 (2010).
  - [10] S. Melcer, H. Hezroni, E. Rand, M. Nissim-Rafinia, A. Skoultschi, C. L. Stewart, M. Bustin, and E. Meshorer, *Nat. Commun.* **3**, 910 (2012).
  - [11] R. Mahen, H. Hattori, M. Lee, P. Sharma, A. D. Jeyasekharan, and A. R. Venkitaraman, *PloS one* **8**, e61893 (2013).

- [12] S. Gilchrist, N. Gilbert, P. Perry, C. Östlund, H. J. Worman, and W. A. Bickmore, *BMC cell Biology* **5**, 1 (2004).
- [13] T. Sullivan, D. Escalante-Alcalde, H. Bhatt, M. Anver, N. Bhat, K. Nagashima, C. L. Stewart, and B. Burke, *J. Cell Biol.* **147**, 913 (1999).
- [14] M. Zhang, C. Seitz, G. Chang, F. Iqbal, H. Lin, and J. Liu, *Cell biology international* **46**, 683 (2022).
- [15] P. Chaudhuri, L. Berthier, and W. Kob, *Phys. Rev. Lett.* **99**, 060604 (2007).
- [16] S. Hapca, J. W. Crawford, and I. M. Young, *J R Soc Interface* **6**, 111 (2009).
- [17] A. V. Chechkin, F. Seno, R. Metzler, and I. M. Sokolov, *Phys. Rev. X* **7**, 021002 (2017).
- [18] E. Barkai and S. Burov, *Phys. Rev. Lett.* **124**, 060603 (2020).
- [19] M. V. Chubynsky and G. W. Slater, *Phys. Rev. Lett.* **113**, 098302 (2014).
- [20] V. Sposini, A. V. Chechkin, F. Seno, G. Pagnini, and R. Metzler, *New J. Phys.* **20**, 043044 (2018).
- [21] Y. Lanoiselée and D. S. Grebenkov, *J. Phys. A* **51**, 145602 (2018).
- [22] W. Wang, A. G. Cherstvy, A. V. Chechkin, S. Thapa, F. Seno, X. Liu, and R. Metzler, *J. Phys. A* **53**, 474001 (2020).
- [23] M. Hidalgo-Soria, E. Barkai, and S. Burov, *Entropy* **23**, 32 (2021).
- [24] K. C. Leptos, J. S. Guasto, J. P. Gollub, A. I. Pesci, and R. E. Goldstein, *Phys. Rev. Lett.* **103**, 198103 (2009).
- [25] B. Wang, S. M. Anthony, S. C. Bae, and S. Granick, *Proc. Natl. Acad. Sci.* **106**, 15160 (2009).
- [26] B. Wang, J. Kuo, S. C. Bae, and S. Granick, *Nat. Mater.* **11**, 481 (2012).
- [27] T. J. Lampo, S. Stylianidou, M. P. Backlund, P. A. Wiggins, and A. J. Spakowitz, *Biophys J.* **112**, 532 (2017).
- [28] J. Janczura, M. Balcerek, K. Burnecki, A. Sabri, M. Weiss, and D. Krapf, *New J. Phys.* **23**, 053018 (2021).
- [29] A. Sabri, X. Xu, D. Krapf, and M. Weiss, *Phys. Rev. Lett.* **125**, 058101 (2020).
- [30] C. Åberg and B. Poolman, *Biophys. J* **120**, 2355 (2021).
- [31] B. Corci, O. Hooiveld, A. M. Dolga, and C. Åberg, *Soft Matter* **19**, 2529 (2023).
- [32] M. Hu, H. Chen, H. Wang, S. Burov, E. Barkai, and D. Wang, *ACS nano* (2023).
- [33] J. Guan, B. Wang, and S. Granick, *ACS Nano* **8**, 3331 (2014).

- [34] J. M. Miotto, S. Pigolotti, A. V. Chechkin, and S. Roldán-Vargas, *Phys. Rev. X* **11**, 031002 (2021).
- [35] R. Pastore, A. Ciarlo, G. Pesce, A. Sasso, and F. Greco, *Soft Matter* **18**, 351 (2022).
- [36] P. S. Laplace, *Stat. Sci.* **1**, 364 (1986).
- [37] S. Burov, S. M. A. Tabei, T. Huynh, M. P. Murrell, L. H. Philipson, S. A. Rice, M. L. Gardel, N. F. Scherer, and A. R. Dinner, *Proc. Natl. Acad. Sci.* **110**, 19689 (2013).
- [38] W. J. T. Bos, B. Kadoch, and K. Schneider, *Phys. Rev. Lett.* **114**, 214502 (2015).
- [39] B. Kadoch, W. J. T. Bos, and K. Schneider, *Phys. Rev. Fluids* **2**, 064604 (2017).
- [40] L. Fang, L. L. Li, J. S. Guo, Y. W. Liu, and X. R. Huang, *Phys. Lett. A* (2022).
- [41] M. Balcerek, A. Pacheco-Pozo, A. Wyłomanska, K. Burnecki, and D. Krapf, arXiv e-prints , arXiv:2407.06374 (2024), arXiv:2407.06374 [cond-mat.stat-mech].
- [42] S. Weber, M. Thompson, W. Moerner, A. Spakowitz, and J. Theriot, *Biophys. J* **102**, 2443 (2012).
- [43] S. Sadegh, J. L. Higgins, P. C. Mannion, M. M. Tamkun, and D. Krapf, *Phys. Rev. X* **7**, 011031 (2017).
- [44] O. Bénichou, C. Loverdo, M. Moreau, and R. Voituriez, *Rev. Mod. Phys.* **83**, 81 (2011).
- [45] A. Weron, K. Burnecki, E. J. Akin, L. Solé, M. Balcerek, M. M. Tamkun, and D. Krapf, *Sci. Rep.* **7**, 5404 (2017).
- [46] K. Pearson, *Nature* **72**, 294 (1905).
- [47] T. Cremer and C. Cremer, *Nat. Rev. Genet.* **2**, 292 (2001).
- [48] K. J. Meaburn and T. Misteli, *Nature* **445**, 379 (2007).
- [49] E. Lieberman-Aiden, N. L. van Berkum, L. Williams, M. Imakaev, T. Ragoczy, A. Telling, I. Amit, B. R. Lajoie, P. J. Sabo, M. O. Dorschner, R. Sandstrom, B. Bernstein, M. A. Bender, M. Groudine, A. Gnirke, J. Stamatoyannopoulos, L. A. Mirny, E. S. Lander, and J. Dekker, *Science* **326**, 289 (2009).
- [50] T. Cremer and M. Cremer, *Cold Spring Harb. Perspect. Biol.* **2**, 2 (2010).
- [51] G. Li, X. Ruan, R. Auerbach, K. Sandhu, M. Zheng, P. Wang, H. Poh, Y. Goh, J. Lim, J. Zhang, H. Sim, S. Peh, F. Mulawadi, C. Ong, Y. Orlov, S. Hong, Z. Zhang, S. Landt, D. Raha, G. Euskirchen, C.-L. Wei, W. Ge, H. Wang, C. Davis, K. I. Fisher-Aylor, A. Mortazavi, M. Gerstein, T. Gingeras, B. Wold, Y. Sun, M. Fullwood, E. Cheung, E. Liu, W.-K. Sung, M. Snyder, and Y. Ruan, *Cell* **148**, 84 (2012).

- [52] S. C. Weber, A. J. Spakowitz, and J. A. Theriot, *Proc. Natl. Acad. Sci.* **109**, 7338 (2012).
- [53] E. R. Weeks, J. C. Crocker, A. C. Levitt, A. Schofield, and D. A. Weitz, *Science* **287**, 627 (2000).
- [54] W. K. Kegel and A. van Blaaderen, *Science* **287**, 290 (2000).
- [55] E. R. Weeks and D. Weitz, *Chem. Phys.* **284**, 361 (2002), strange Kinetics.
- [56] I. Chakraborty and Y. Roichman, *Phys. Rev. Research* **2**, 022020 (2020).
- [57] M. Lavaud, T. Salez, Y. Louyer, and Y. Amarouchene, *Phys. Rev. Research* **3**, L032011 (2021).
- [58] L. Luo and M. Yi, *Phys. Rev. E* **97**, 042122 (2018).
- [59] L. Luo and M. Yi, *Phys. Rev. E* **100**, 042136 (2019).
- [60] E. B. Postnikov, A. Chechkin, and I. M. Sokolov, *New J. Phys.* **22**, 063046 (2020).
- [61] A. Pacheco-Pozo and I. M. Sokolov, *Phys. Rev. Lett.* **127**, 120601 (2021).
- [62] F. Baldovin, E. Orlandini, and F. Seno, *Front. Phys.* **7**, 124 (2019).
- [63] M. Hidalgo-Soria and E. Barkai, *Phys. Rev. E* **102**, 012109 (2020).
- [64] S. Nampoothiri, E. Orlandini, F. Seno, and F. Baldovin, *Phys. Rev. E* **104**, L062501 (2021).
- [65] S. Nampoothiri, E. Orlandini, F. Seno, and F. Baldovin, *New J. Phys.* **24**, 023003 (2022).
- [66] W. Wang, E. Barkai, and S. Burov, *Entropy* **22**, 22 (2020).
- [67] F. Thiel, L. Schimansky-Geier, and I. M. Sokolov, *Phys. Rev. E* **86**, 021117 (2012).
- [68] J. Taktikos, H. Stark, and V. Zaburdaev, *PLOS ONE* **8**, 1 (2014).
- [69] S. Fedotov, D. Han, A. O. Ivanov, and M. A. A. da Silva, *Phys. Rev. E* **105**, 014126 (2022).
- [70] U. Basu, S. N. Majumdar, A. Rosso, and G. Schehr, *Phys. Rev. E* **98**, 062121 (2018).
- [71] S. N. Majumdar and B. Meerson, *Phys. Rev. E* **102**, 022113 (2020).
- [72] K. Malakar, A. Das, A. Kundu, K. V. Kumar, and A. Dhar, *Phys. Rev. E* **101**, 022610 (2020).
- [73] V. Zaburdaev, S. Denisov, and J. Klafter, *Rev. Mod. Phys.* **87**, 483 (2015).
- [74] K. Kanazawa, T. G. Sano, A. Cairoli, and A. Baule, *Nature* **579**, 364 (2020).
- [75] X. Wang, Y. Chen, and W. Deng, *Phys. Rev. Research* **2**, 013102 (2020).
- [76] D. Han, M. A. A. da Silva, N. Korabel, and S. Fedotov, *Phys. Rev. E* **103**, 022132 (2021).
- [77] S. Mukherjee, R. K. Singh, M. James, and S. S. Ray, *Phys. Rev. Lett.* **127**, 118001 (2021).
- [78] C. Bechinger, R. Di Leonardo, H. Löwen, C. Reichhardt, G. Volpe, and G. Volpe, *Rev. Mod. Phys.* **88**, 045006 (2016).
- [79] R. Jeanneret, D. O. Pushkin, V. Kantsler, and M. Polin, *Nat. Commun.* **7**, 12518 (2016).
- [80] S. Ro, Y. Kafri, M. Kardar, and J. Tailleur, *Phys. Rev. Lett.* **126**, 048003 (2021).

[81] Y. Lanoiselée and D. S. Grebenkov, Phys. Rev. E **96**, 022144 (2017).